

Intrinsically Photopatternable High-k Polymer Dielectric for Flexible Electronics

Gunoh Lee, Seong Cheol Jang, Ju Hyeok Lee, Ji-Min Park, Byeongil Noh, Hyuk Choi, Hyukmin Kweon, Do Hwan Kim, Hyun You Kim,* Hyun-Suk Kim,* and Kyung Jin Lee*

The development of flexible and stretchable devices is crucial for realizing future electronics. In particular, for dielectric layer, conventional inorganic materials are limited by their brittle nature, while organic materials suffer from a low dielectric constant. Here, a novel intrinsically photopatternable high-k Parylene-based thin film (Parylene-OH) is fabricated via a chemical vapor deposition process based on the Gorham method, which provides pin-hole free, conformal polymeric film on any type of surface. Parylene-OH can be photo-patterned by UV crosslinking without further lithography processes and dielectric constant of Parylene-OH increases from 6.05 to 7.53 after crosslinking, without degrading other parameters, making it comparable to conventional high-k dielectric, Al_2O_3 . Flexible In–Ga–Zn–O (IGZO) thin-film transistors (TFTs) with patterned dielectric layers can withstand higher strain owing to the localized pattern of each unit. A CMOS inverter integrated with n-type IGZO and p-type Te TFTs is successfully fabricated. Parylene-OH can be used in the future of state-of-the-art flexible electronic devices.

1. Introduction

Thin-film transistors (TFTs) are one of the vital units in electronic devices, and their importance is increasing owing to growing demands of the modern digital era. Each component of TFT devices, such as semiconductors, gate dielectrics, and their architecture, has been extensively investigated to realize high-performance TFT devices. In particular, diverse materials beyond silicon-based semiconductors (either n- or p-type), such as oxides, perovskites, and organic semiconductors, have been examined to replace conventional Si active layers.^[1–5] Additionally, among the various gate-insulating layers that have been investigated, oxide-insulating layers (silica or alumina, etc.) are commonly adopted in most TFT devices owing to their excellent insulating properties, stabilities, and interfacial

characteristics.^[6–9] However, there have been several problems in terms of their characteristics and processability; for instance, it is difficult to realize top-gated TFT devices using conventional oxide insulating layers owing to possible damage of the active layer during harsh processing conditions, whereas a top-gated insulating layer can act as an additional encapsulation or protective layer. Moreover, the oxide-insulating layers are inherently brittle, which poses a critical limitation in the development of flexible and stretchable devices.^[10–12]

The growing demand for flexible and stretchable electronic devices has led to increased research on the development of organic or polymeric-based flexible insulating layers. Although polymeric layers offer several advantages in terms of processing (solution processability and low costs) and physical attributes (flexibility, durability, and stretchability), they require extremely thin dielectric layers owing to the intrinsic low-dielectric constant of organic materials, which results in a low driving current. On the other hand, there are several studies on high-k dielectric, including inorganic, and organic materials.^[13–21] Inorganic materials have advantages such as excellent dielectric properties, low leakage current, and large breakdown field, but their brittle nature is not suitable for next-generation flexible and stretchable electronics.^[15,22–26] Organic materials have recently been receiving a lot of research into the dielectric layer of future flexible and stretchable TFT based on their excellent physical properties. Recently, a number of polymer dielectrics with dielectric constants exceeding 10 or showing very low leakage current density have

G. Lee, B. Noh, K. J. Lee
Department of Chemical Engineering and Applied Chemistry
Chungnam National University
Daejeon 34134, Republic of Korea
E-mail: kjlee@cnu.ac.kr

S. C. Jang, J.-M. Park, H.-S. Kim
Department of Energy and Materials Engineering
Dongguk University
Seoul 04620, Republic of Korea
E-mail: khs3297@dongguk.edu

J. H. Lee, H. Choi, H. Y. Kim, H.-S. Kim
Department of Materials Science and Engineering
Chungnam National University
Daejeon 34134, Republic of Korea
E-mail: kimhy@cnu.ac.kr

H. Kweon, D. H. Kim
Department of Chemical Engineering
Hanyang University
Seoul 04763, Republic of Korea

D. H. Kim
Institute of Nano Science and Technology
Hanyang University
Seoul 04763, Republic of Korea

D. H. Kim
Clean-Energy Research Institute
Hanyang University
Seoul 04763, Republic of Korea

The ORCID identification number(s) for the author(s) of this article can be found under <https://doi.org/10.1002/adfm.202405530>

DOI: 10.1002/adfm.202405530

been reported. However, most of them are manufactured based on a solution process, which has inevitable side effects, such as void, pinhole, and coffee ring effects, which are not suitable for cutting-edge electronics. In addition, it is difficult to obtain pin-hole-free thin polymeric films via solution processing.^[27,28] As an alternative, the vapor-processable introduction of polymeric layers is a promising approach, and outstanding results have been reported recently.^[29–31] Parylene-based polymers are well-established vapor-processable polymers^[32–35] and several attempts have been made to apply Parylene films as a gate dielectric layer.^[36–38] Our recent work has proven the possibility of applying diverse Parylene polymers in the organic dielectric layers of top-gated TFT devices based on various oxide semiconductors.^[5,39] To the best of our knowledge, no specific interface mismatches, roughness problems, or pinhole problems have been observed, regardless of the type of active layer, using various types of Parylene derivatives, including synthesized/functionalized dimers.

The development of patternable dielectric layers has recently attracted significant attention. The patterned and isolated dielectric layer can provide advantages in terms of device performance by reducing parasite capacitance and RC delays and enables us to consider stretchable devices by the localized pattern of each unit. Since patterning of the dielectric layer by a shadow mask has an intrinsic limitation in resolution, the only possible method is the introduction of an additional photolithography process during device fabrication, which can incur excessive cost increments and complicate the fabrication process. Therefore, there have been several attempts to use photoreactive polyimides or add photo additives to polymeric insulators for preparing photopatternable dielectric layers.^[40–45] However, the above-mentioned problems associated with solution-processable dielectric layers should be addressed for practical applications.

In this work, we report on the application of Parylene-based (vapor process enabled) photopatternable polymeric gate dielectric layers on oxide semiconductor TFT devices. Hydroxy-functionalized paracyclophane dimers can produce pin-hole-free conformal polymeric thin films on any substrate. Similar to our previous works, the functionalized Parylene (hereinafter referred to as Parylene-OH) film exhibits excellent performance as a gate dielectric layer. The Parylene-OH demonstrates superior dielectric constant (6.05 (pristine), 7.53 (crosslinked) at 100 kHz) to commercialized Parylene films (Parylene-C 2.91, Parylene-D 2.58, Parylene-AF4 2.95 at 100 kHz)^[5]; thus, high driving current values can be obtained. Further, an additional photoreaction enables the material to be applied to the photopatternable dielectric layer. The transfer characteristics were maintained after UV irradiation, even after the development process. Flexible TFT devices were fabricated using the developed photopatternable dielectric layers. Finally, a complementary metal-oxide semiconductor (CMOS) inverter was fabricated to demonstrate further applications. These vapor-processable and photopatternable polymeric dielectric layers can provide evolutionary breakthroughs in next-generation electronic devices.

2. Results and Discussion

Figure 1a presents an overall schematic diagram showing the preparation of TFTs devices using In–Ga–Zn–O (IGZO) and photopatternable organic dielectric layers. First, the IGZO ac-

tive layer was sputtered on a glass substrate, followed by rapid thermal annealing (RTA) at 300 °C. Upon depositing the Al source/drain (S/D) via a thermal evaporation system, an organic dielectric layer was deposited using the Gorham method, as shown in **Figure 1b**.^[46] This process can be easily accessible because the CVD of Parylene-OH is also available using commercial coater by just changing dimer. The activated monomer from a dimer called 4-hydroxy[2.2]paracyclophane was involved in polymerization over the entire area of the TFT array, providing the polymeric thin film, as shown in **Figure 1c**. The sublimed monomer is fed into pyrolysis zone (typically 550–560 °C) using argon carrier gas (the flow rate and sublime temperature is controlled to maintain vacuum pressure of chamber ≈ 0.1 – 0.15 torr during entire process, and the growth yield was in this process was 0.32 nm mg^{-1}). As shown in **Figure 1b**, photopatterned organic dielectrics were realized by UV crosslinking at 254 nm for 10 min using a photomask followed by developing with THF solvent, which is a relatively simple process compared to photolithography using a photoresist. Finally, the Al gate electrode was fabricated via thermal evaporation. Detailed experimental parameters of the fabrication and photopatterning process are described in the Experimental Section.

2.1. Characterization of Parylene-OH and Oxide TFT

To deposit the Parylene-OH film via chemical vapor deposition (CVD) polymerization, poly[(hydroxy-*p*-xylylene)-co-(*p*-xylylene)], the dimer was synthesized in two steps from the commercialized dimer [2.2]paracyclophane.^[47] The synthetic process is not quite complicate, and thus the cost of synthetic monomer will be much cheaper than the most expensive Parylene dimer (i.e., Parylene-AF4, high-performance parylene dimer available in market). The vapor phase coating of Parylene-OH was conducted in a pressure of ≈ 0.10 to 0.15 Torr on a deposition holder which was cooled down to 5 in an 80 °C chamber passing through the pyrolysis region ≈ 550 – 560 °C (see details in Experimental Section). **Figure 2a** illustrates the chemical structure and Fourier-transform infrared (FTIR) spectra of the dimer and polymer of Parylene-OH, respectively, revealing O–H stretching at 3500 – 3200 cm^{-1} , C–H stretching at $\approx 2900 \text{ cm}^{-1}$, and C–C/C=C stretching band composing the aromatic ring at $\approx 1500 \text{ cm}^{-1}$. The detailed synthetic scheme of the dimer is described in **Figure S1a** (Supporting Information). Moreover, the successful synthesis of the dimer was confirmed by ^1H - and ^{13}C -NMR spectroscopic analyses (**Figure S1b–e**, Supporting Information). Detailed NMR analysis data is provided in the experimental Section. Unlike common liquid-based processes, Parylene-OH can be polymerized via CVD, resulting in conformal films with a good surface roughness of RMS value below 1 nm on any substrate, including the IGZO and Si substrates, as presented in **Figure 2b**. CVD processes for Parylene can provide a good interface match as well as high-quality polymeric thin films regardless of the substrate.^[5] Cross-sectional images of IGZO TFTs from FIB-SEM confirmed that Parylene-OH has no pinholes, voids, or any mismatches between organic and inorganic materials for each layer in the TFT architecture, as shown in **Figure 2c**.

The dielectric and electrical properties of Parylene-OH were measured using metal-insulator-metal (MIM) devices. **Figure 2d**

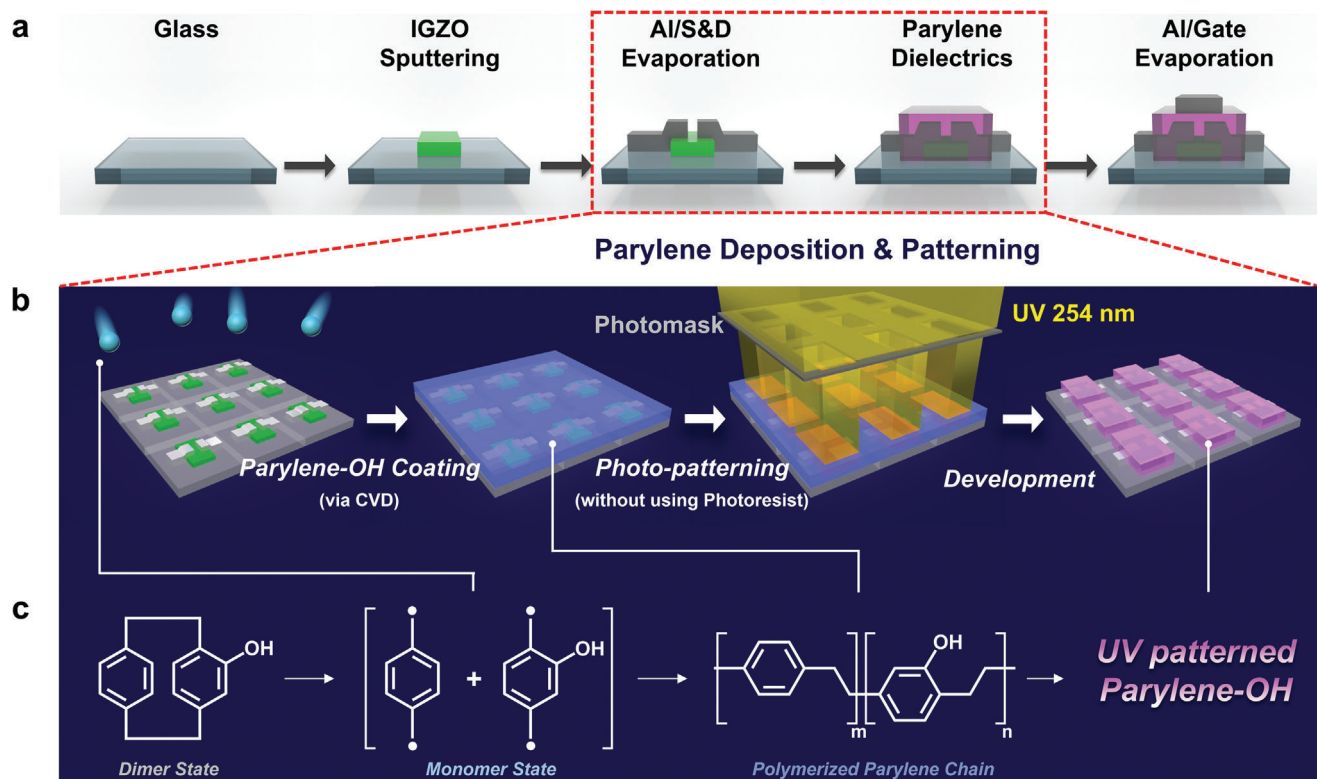


Figure 1. Overall process of fabricating the top-gated IGZO TFT device and photopatterning process of Parylene-OH. a) Schematics of fabricating the top-gated thin film transistor. b) Detailed process of fabricating patterned-Parylene dielectrics depicting the photopatterning steps. The Parylene-OH was deposited on the entire area of the TFT array via CVD based on the Gorham method. Thereafter, the localized Parylene-OH could be implemented with subsequent developing steps via the photo-crosslinking process using photomask and UV 254 nm. c) Chemical structure representation of polymerizing Parylene-OH in each step.

illustrates the capacitance–voltage curves of Parylene-OH from -5 to 5 V at 100 kHz (as a comparison, MIM analysis of Parylene-C is presented as a dashed line). Although most commercial polymers, including commercialized Parylene, have dielectric constants below 5 , such as poly(methyl methacrylate) ($k = 3.5$), poly(vinyl phenol) ($k = 4.2$), polystyrene ($k = 2.6$), Parylene-C ($k = 2.9$), Parylene-D ($k = 2.6$), Parylene-N ($k = 2.6$), and Parylene-AF4 ($k = 2.9$), Parylene-OH fabricated via CVD polymerization exhibits capacitance values (53 nF cm^{-2} , $\epsilon_r = 6.05$ at 100 kHz) that are significantly higher than those of commercial polymers and more than double those of the conventional Parylene family.^[48–50] Figure S2 (Supporting Information) shows the frequency-dependent dielectric properties of Parylene-OH under frequency of 1 kHz to 1 MHz, which consists of voltage sweep capacitance of Parylene-OH. Because the CVD process is relatively robust over large areas, the uniformity of 20 MIM devices is good, as shown in Figure S2b (Supporting Information). Additionally, there is no specific deterioration in dielectric and electrical properties when film thickness is reduced to 50 nm as shown in Figure S2c–e (Supporting Information). The high dielectric properties of Parylene-OH may be related to the functional group of Parylene-OH and the hydroxy group ($-\text{OH}$). The dielectric properties represent the ability of a material to store electrical energy in response to an external electric field and are influenced by the polarity of the material. The hydroxy group is known to have a high dipole moment compared to fluorine (Parylene-AF4) and

chlorine functional groups (Parylene-C, Parylene-D). The leakage current density of Parylene-OH was below $10^{-9} \text{ A cm}^{-2}$ at 1 MV cm^{-1} and showed no dielectric breakdown until the breakdown field of 3 MV cm^{-1} , as depicted in Figure 2e, revealing the excellent electrical and dielectric properties of Parylene-OH.

Figure 2f illustrates the transfer curves of IGZO TFTs prepared with Parylene-OH and Parylene-C for comparison (thickness of the dielectric layer: 100 nm). IGZO TFTs with Parylene-OH exhibit mobility, subthreshold swing, turn-on voltage, on/off ratio, and interface trap density of $7.61 \text{ cm}^2 \text{ V}^{-1} \text{ s}^{-1}$, 0.26 V dec^{-1} , -0.91 V , $> 10^7$ and $1.13 \times 10^{12} \text{ V}^{-1} \text{ cm}^{-2}$ respectively. Owing to the higher capacitance of Parylene-OH compared to Parylene-C ($\epsilon_r = 2.83$ at 100 kHz), IGZO TFTs with a Parylene-OH gate dielectric exhibit more than two times higher drain current. Also, IGZO TFT with Parylene-OH shows almost no hysteresis as shown in Figure 2g, indicating that the interface between the semiconductor and dielectric is excellent. Positive bias stress (PBS) and negative bias stress (NBS) tests of the fabricated IGZO TFTs with Parylene-OH also confirmed the electrical stability of the IGZO TFTs. The applied gate voltage (V_G) and drain voltage (V_D) were ± 10 and 0.1 V, respectively. Each stability test was conducted at room temperature (RT, 25°C) in air and dark for 1 h. Here, PBS and NBS of IGZO TFTs with Parylene-OH show ΔV_{on} values of 0.56 and -1.11 V, respectively, as shown in Figure 2h (see Figure S3, Supporting Information for detailed transfer curves). In addition, IGZO TFTs with Parylene-OH show

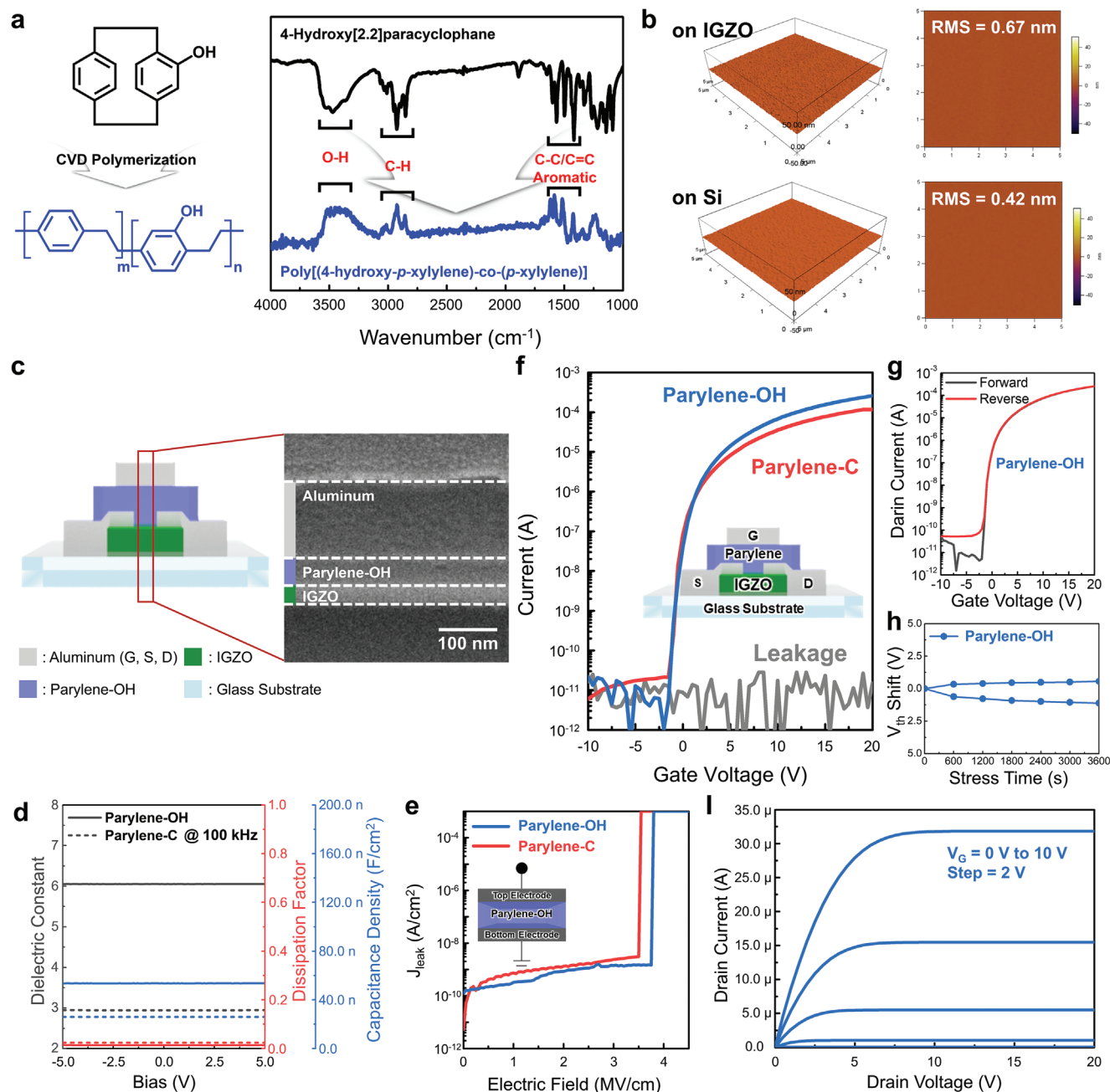


Figure 2. Parylene-OH dielectric polymer and its TFTs device. a) Chemical structure of dimer and polymer state of Parylene-OH for each, as well as the FTIR spectra sustaining the functional group on the polymer even after the CVD polymerization. b) Surface roughness of Parylene-OH thin film on the various substrates including oxide and Si wafer. c) Schematic image of top-gate TFTs using Parylene-OH as gate dielectric and its cross-sectional FIB-SEM image, showing interfaces of each layer. d) Dielectric properties of parylene-OH at 100 kHz (parylene-C for comparison) e) J_{leak} -E-field characteristics of MIM devices with different parylene dielectrics f) Transfer curves of IGZO TFTs with different gate dielectrics, obtained from V_{DS} of 10 V g) Hysteresis, h) NBS and PBS stability, and i) Output curves of IGZO TFTs with Parylene-OH.

good output curves with no current crowding and ohmic-like contact, as shown in Figure 2i. The results indicate that Parylene-OH can be applied to IGZO TFTs as an organic dielectric layer without any specific problems. These results indicate that Parylene films polymerized from the Parylene derivatives can be successfully adopted as a gate dielectric layer, as described in our previous results.^[5]

2.2. UV Crosslinkable Parylene Dielectric Layer and TFTs Applications

The Parylene family is well known for its excellent chemical resistance and non-solubility in any organic solvent owing to their extremely high molecular weight.^[51] However, in the case of Parylene-OH, the film can be dissolved in tetrahydrofuran

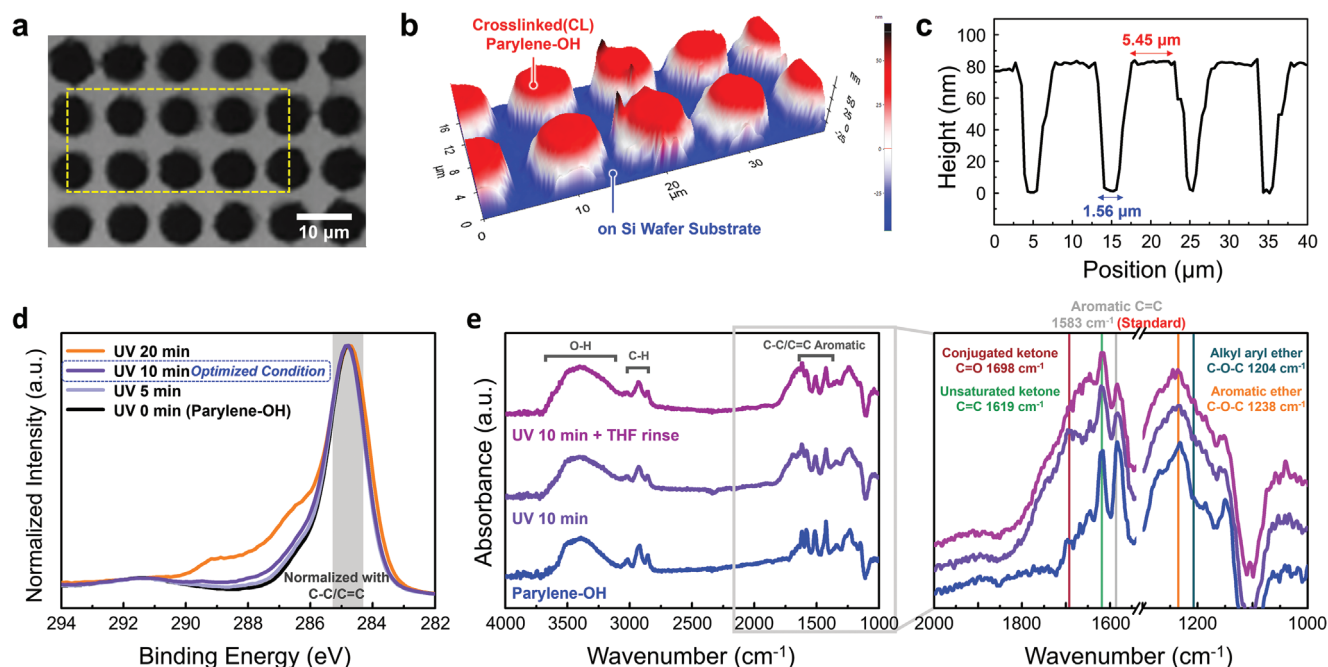


Figure 3. UV Crosslinkable Parylene Dielectric Layer. a) OM image of 5 μm scale island-patterned Parylene-OH. b) AFM 3D topology showing the boundaries of the crosslinked Parylene-OH (red) on the Si wafer substrate (blue). c) Line profile information of height to position from island-patterned of Figure 2b. d) XPS spectra according to UV irradiation time for the carbon species. e) FTIR spectra for the overall molecular structure at each photopatterning step and its detailed analysis below 2000 cm^{-1} .

(THF). Considering this soluble property against a specific solvent, unlike the conventional Parylene, the Parylene-OH polymer may have a relatively lower molecular weight (however, it has a sufficiently high molecular weight that can serve as a dielectric layer, as indicated above). Note that Parylene-OH exhibits the unique characteristic of being capable of crosslinking via exposure to UV irradiation at a wavelength of 254 nm, changing its properties from THF soluble to insoluble (Figure S4, Supporting Information). Therefore, UV photopatterning of Parylene-OH was achieved by developing unexposed Parylene-OH using THF, as shown in Figure 3a. In this study, photopatterning was demonstrated at a resolution of 5 μm scales with island shape patterned array on Si wafer substrate (Figure 3a). Figure 3b shows the 3D AFM topology of UV crosslinked Parylene-OH (hereafter referred to as “CL Parylene-OH”), and the cross-sectional height profile shows CL Parylene-OH can be patterned in the resolution of $\approx 5\text{ }\mu\text{m}$ at intervals of $\approx 1.5\text{ }\mu\text{m}$, as shown in Figure 3c. Furthermore, it is possible to make patterns in various forms, including simple repeating patterns (islands) and custom-designed letter-shaped patterns (such as “S”), as illustrated in Figure S5 (Supporting Information). CL Parylene-OH can provide high-resolution and sharp boundaries of patterns via a simple fabrication process involving UV treatment and development. Therefore, it is a promising alternative to photoresist-based patterning of dielectrics, which typically involves highly complex fabrication processes. Furthermore, as demonstrated in Figure S6 (Supporting Information), the surface roughness of CL Parylene-OH remains largely unaltered after the development process, suggesting that it is a highly reliable material for various applications. In addition, looking at Figure S7 (Supporting Information), it can

be confirmed through FIB-SEM analysis to see the cross-section of the MIM structure that the Parylene-OH has little change in thickness and maintains a good initial interface state for each step of patterning. Prolonged exposure of most polymer films to UV radiation at a wavelength of 254 nm can lead to oxidation and chain scissoring.^[52] For the hydroxy functional group in phenol, UV radiation at a wavelength of 254 nm can cause the formation of phenol radicals, which can create additional active sites for crosslinking.^[53] Figure 3d illustrates the XPS spectra of the Parylene-OH films according to the UV exposure time.

As described in the detailed analysis of the C1s peak with deconvolution (Figure S8, Supporting Information), there are obvious differences in the oxidation behavior between Parylene-C and Parylene-OH. In the case of non-phenol species (Parylene-C), surface oxidation occurs immediately after UV irradiation (Figure S8d–f, Supporting Information).^[54,55] However, the polymers with phenol species (Parylene-OH, Figure S8a–c, Supporting Information) withhold oxidation until 10 min of UV irradiation, which could be attributed to active radical formation. However, note that if the UV irradiation time exceeds 10 min, an increase in the C=O peak intensity and the appearance of O–C=O peaks are observed owing to the oxidation of the polymer film like Parylene-C. Hence, we selected 10 min of UV irradiation as the optimum condition for crosslinking the Parylene-OH while preventing over-oxidation. The surface modulus of both Parylene-OH and the crosslinked films was even higher than that of the conventional Parylene-C, indicating that our designed Parylene-OH provides enhanced mechanical strength (Figure S9, Supporting Information).^[56] Note that, the obtained film modulus of the

Parylene-OH family surpassed that of previously reported polymer films which are conventionally used in the field of polymer electronics.^[57,58]

The FTIR spectra in Figure 3e demonstrate that the overall molecular structures are maintained after UV irradiation and development. However, compared to the internal standard (C=C of benzene at 1583 cm⁻¹), the C=O stretching of conjugated ketone and the C=C stretching of unsaturated ketone at 1698 and 1619 cm⁻¹ are slightly increased. Furthermore, there is a slight increase in two types of ether peaks, C—O—C aromatic ether at 1238 cm⁻¹ and alkyl aryl ether at 1204 cm⁻¹, suggesting that the single-linear chain structure of Parylene-OH is converted to a multi-crosslinked chain structure following the UV crosslinking process. The phenol radical is formed by 254 nm UV irradiation, which has a resonance structure for the localization of the radical. Also, there are carbons that are susceptible to being attacked by other radical species including partially negative sites. This mechanism is presented in detail in Figure S10a,b (Supporting Information).

Although further structural analysis of CL Parylene-OH is needed, it was challenging to characterize the polymer state (thin film) due to its high resistance to organic solvents typically used for analyses. As an alternative approach, indirect evidence was obtained by UV curing the dimer state rather than the polymer state, as the dimer state is soluble in organic solvents even after photoreaction. Figure S11 (Supporting Information) suggests characterization of Parylene-OH in the form of multiple units of dimer. TLC plate analysis reveals a new small peak after UV irradiation on dimer, which can be confirmed again by ¹³C-NMR spectroscopy. Moreover, the FTIR spectra of photo-irradiated dimers showed a similar trend as shown in Figure 3e. Through this evidence, the final chemical structure of CL Parylene-OH could be expected to be depicted as shown in Figure S10c (Supporting Information).

The morphologies of the DFT-optimized multi-stacked Parylene-OH and CL Parylene-OH show that the spatial density (packing density) increases during the crosslinking because of the formation of the short —C—O—C— bonds (Figure 4a,b). The calculated static dielectric constant (ϵ_{static} , sum of electronic and ionic dielectric constants) using the density functional perturbation theory (DFPT) confirms that the ionic dielectric constant significantly increased after cross-linking. The calculated ϵ_{static} of CL Parylene-OH was 7.86, almost consistent with the experimental value of 7.53. The DFT-calculated total dipole moments along the lattice directions confirm that the crosslinking increases the dipole moment of Parylene-OH along the plane in which the —C—O—C— bonds are aligned (Figure 4a,b). Figure 4c summarizes the experimental data and DFPT calculation data of the dielectric constants of the two materials. The sliced electron density maps also present the enriched electron density along the —C—O—C— bonds, which generate local dipole moments (Figure S12, Supporting Information).

The dielectric and electric properties of the CL Parylene-OH and Al₂O₃ films are shown in Figure 4d,e. The Al₂O₃ films were fabricated via plasma-enhanced atomic layer deposition (PEALD) for comparison. The MIM structure capacitor devices were confirmed to be fully working after solvent development, showing an

increased dielectric constant of 7.53 at 100 kHz, similar to that of the well-known high-k Al₂O₃ dielectric fabricated via PEALD. Steady dielectric properties over wide ranges of frequency and voltage indicate that the patterning process has no fatal effect on insulating performances, as shown in Figure S13a (Supporting Information). Also as shown in Figure S2b (Supporting Information), 20 MIM devices with CL Parylene-OH show good area uniformity. No degradation in dielectric and electrical properties of CL Parylene-OH was observed when the film thickness was reduced to 50 nm, the same as Parylene-OH, as shown in Figure S13b–d (Supporting Information). Note that the dielectric constant of CL Parylene-OH increases from 6.05 to 7.53, which is a significant improvement. Because the reduction amount of —OH groups after crosslinking is marginal (see FTIR, Figure 3e), the increment of the dielectric constant after crosslinking is primarily due to the formation of a short C—O—C bond. In addition, the bandgap of Parylene-OH before and after UV crosslinking was measured as 4.17 and 3.91 eV, respectively through the Tauc plot from UV-vis analysis (Figure S14, Supporting Information).

Despite undergoing the patterning process, CL Parylene-OH exhibits a similar breakdown field over 3 MV cm⁻¹ compared to Parylene-OH and a low leakage current density of 2.6×10^{-9} A cm⁻² at an electrical field of 1 MV cm⁻¹, indicating no additional damage to the dielectric layer during the patterning process. The leakage current density of CL Parylene-OH increases by 1 order of magnitude compared to that of Parylene-OH, mainly due to lowering bandgap (Figure S14, Supporting Information) and corresponding to the large increment in dielectric constant. Moreover, the low leakage current density can be attributed to several factors, including the inhibition of ion migration, reduced free volume, and non-pinhole surface morphology of the crosslinked copolymers. IGZO TFTs fabricated with CL Parylene-OH show mobility, subthreshold swing, turn-on voltage, on/off ratio, and interface trap density of 9.22 cm² V⁻¹s⁻¹, 0.41 V dec⁻¹, 0.70 V, > 10,⁷ and 2.41×10^{12} V⁻¹cm⁻² respectively (Figure 4f). The top-gate IGZO TFTs using PEALD Al₂O₃ show mobility, subthreshold swing, turn-on voltage, on/off ratio, and interface trap density of 8.51 cm² V⁻¹s⁻¹, 0.56 V dec⁻¹, -0.73 V, > 10,⁷ and 3.11×10^{12} V⁻¹cm⁻² respectively. IGZO TFTs with CL Parylene-OH show a high driving current equal to the existing high-k inorganic Al₂O₃ gate dielectrics, indicating that CL Parylene-OH can act as a high-k gate dielectric in IGZO TFTs. There is no specific hysteresis between forward and reverse scans as indicated in Figure S15 (Supporting Information). The output curves exhibit ohmic-like contacts and no current crowding, indicating a good interface between IGZO and CL Parylene-OH (Figure 4g). To evaluate the electrical stability of the IGZO TFT, the PBS/NBS test on the IGZO TFT with CL Parylene-OH was conducted under the same conditions as the IGZO TFT with parylene-OH mentioned above. Figure 4h shows the evolution of the turn-on voltage as a function of time of IGZO TFTs with CL Parylene-OH and PEALD Al₂O₃. PBS and NBS of CL Parylene-OH show ΔV_{on} values of 0.52 and -1.12 V, respectively, which are comparable to those of above mentioned IGZO TFTs with Parylene-OH and the previously reported IGZO TFTs with Parylene-C gate dielectrics.^[5] However, IGZO TFTs with PEALD Al₂O₃ in this study exhibit a significantly large V_{on} shift of more than ± 2 V in both PBS and NBS tests, which might be because of damages caused by the

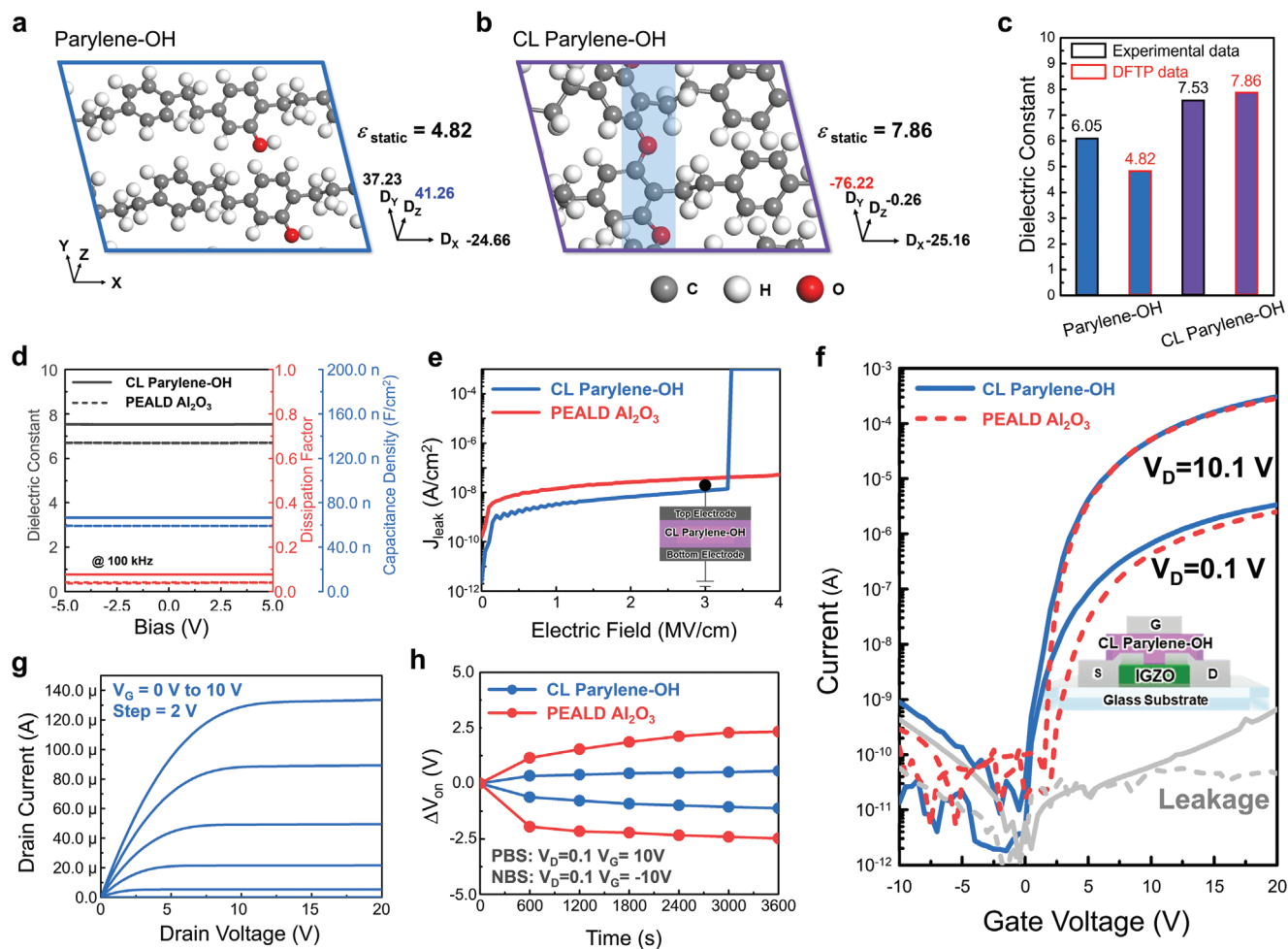


Figure 4. CL Parylene-OH, thin films, and transistor. DFT-optimized morphology of a) Parylene-OH and b) CL Parylene-OH. The DFT-estimated static dielectric constant (ϵ_0) is presented along. The numbers with the axes present the total (electronic+ionic) dipole moment along the directions. c) Comparison of a dielectric constant between experimental value and calculated static dielectric constant. d) Dielectric properties of crosslinked parylene-OH at 100 kHz (PEALD Al_2O_3 for comparison) e) leakage current density of crosslinked Parylene-OH and PEALD Al_2O_3 f) Representative transfer curves of IGZO TFTs with crosslinked Parylene-OH and PEALD Al_2O_3 g) Output curves of IGZO TFTs with crosslinked Parylene-OH h) Electrical stability of IGZO TFTs with different gate dielectrics.

plasma applied to the IGZO active layer during the dielectric deposition process. All the above results indicate again the stability of Parylene-OH against environments such as exposure to UV and external chemicals during development and drying process. Additionally, we have checked thermal stability of Parylene-OH and CL Parylene-OH by MIM test (Figure S16, Supporting Information). Although there are little changes in dielectric properties of Parylene-OH with increasing temperature, those of CL Parylene-OH show negligible differences, meaning higher thermal stability after UV crosslinking. Conduction mechanism of parylene families has been known as the bulk-limited mechanism, mainly based on hopping conduction related to the bulk trap sites.^[59–62] CL parylene OH showed improved stability of leakage current with temperature variations, which may be due to the mitigated presence of bulk trap states compared to parylene OH.

2.3. Flexible Device and CMOS Inverter Using Patternable Parylene

Flexible TFTs were fabricated on a PI substrate to demonstrate the advantages of dielectric patterning. Because the temperature of the target surface should be maintained at 5 °C, there is no thermal damage on a PI substrate during CVD. To avoid the penetration of gas from the PI substrate, 50 nm thick Al_2O_3 was deposited as a buffer layer via PEALD.^[10,63–65] The schematic structures of flexible IGZO TFTs with patterned and non-patterned gate dielectrics are shown in Figure 5a. Meanwhile, Figure 5b illustrates the transfer curves of the flexible IGZO TFTs with patterned and non-patterned CL Parylene-OH. IGZO TFTs with patterned and non-patterned CL Parylene-OH were successfully fabricated and confirmed to exhibit typical transistor characteristics. The mechanical stability of the flexible IGZO TFTs was evaluated

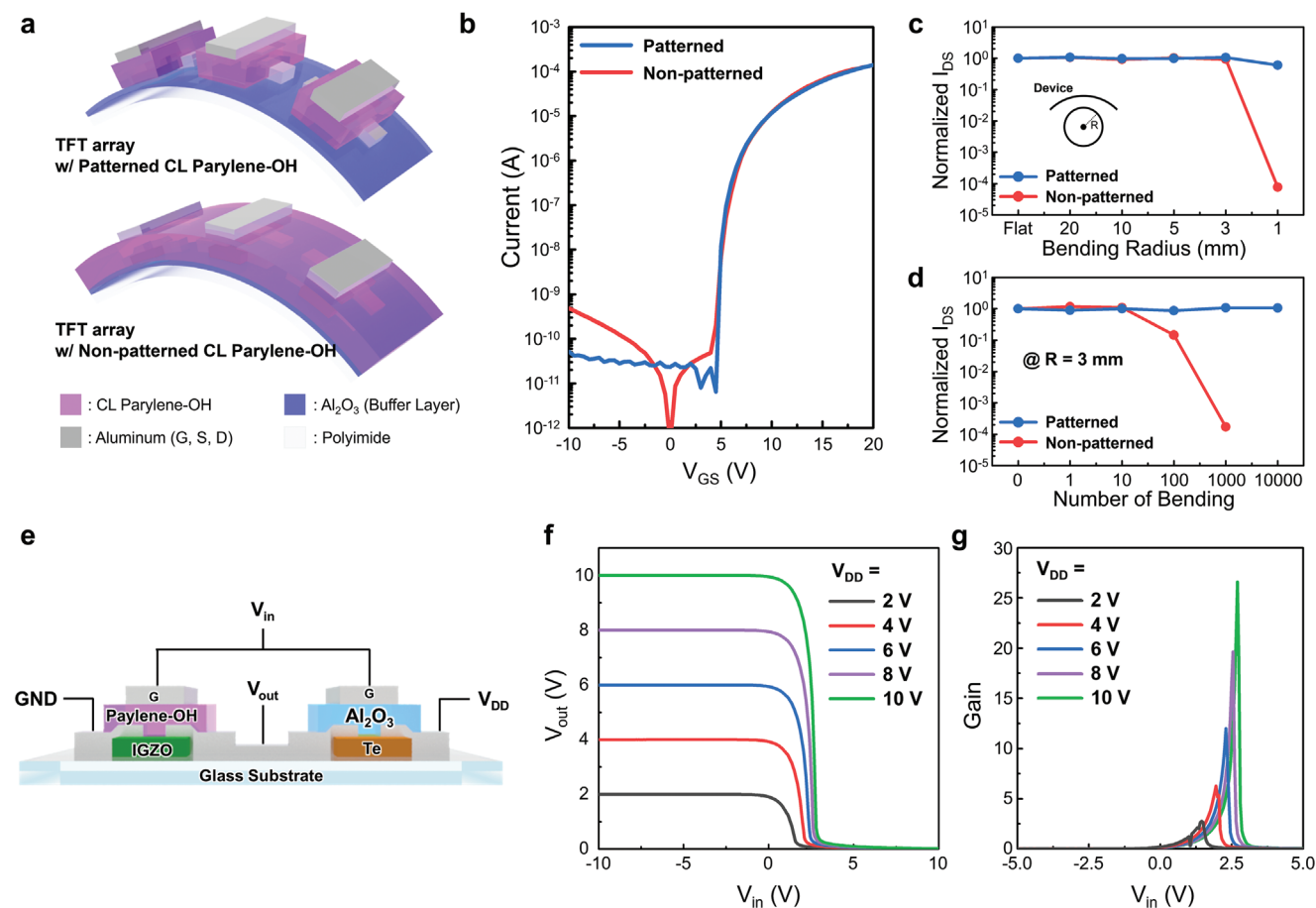


Figure 5. Flexible device and CMOS inverter using patternable-Parylene. a) Schematic structure of the fabricated TFT array using patterned and non-patterned CL Parylene-OH. b) Transfer curves of the flexible IGZO TFTs comparing two types of TFT arrays. c,d) Evolution of the normalized drain current as a function of bending radius c) and number of bending d). e) Schematic layout of fabricated CMOS inverter using an n-type IGZO and p-type Te. f,g) Voltage transfer f) and gain characteristics of the CMOS inverter g).

with different bending radii and bending numbers. The evolution of the normalized drain current as a function of the bending radius and number of bends is shown in Figure 5c,d, respectively. The strains of the bending test were calculated by following the formula; $\epsilon = h/2R$, here ϵ , h , and R were strain, thickness, and bending radius respectively. In a varying bending radius test, the non-patterned IGZO TFTs were found to exhibit a stable normalized drain current up to a bending radius of 3 mm ($\approx 1.75\%$). However, it appears that at a bend radius of 1 mm ($\approx 5.25\%$), the non-patterned IGZO TFTs exhibit abnormal behavior, with the drain current decreasing significantly by approximately five orders of magnitude. This suggests that the devices cannot withstand such a harsh bending radius without significant degradation of their electrical properties. In contrast, the patterned IGZO TFTs appear to be more resilient to bending, with a slight decrease in the normalized drain current compared with TFTs with non-patterned gate dielectrics. This suggests that the patterned dielectrics of IGZO TFTs can enhance their flexibility and resistance to bending, potentially making them more suitable for use in flexible or wearable electronic devices. Additionally, bending tests were conducted with varying numbers of bends to evaluate the performance of both patterned and non-patterned TFTs at a

bending radius of 3 mm, where both types of TFTs exhibit normal transfer characteristics. The results of the bending test for the TFT with the non-patterned dielectric layer indicate that the normalized drain current decreases significantly over time as the number of bending cycles increases. Specifically, after 100 bending cycles, the normalized drain current decreases by an order of magnitude, and after 1000 bending cycles, the decrease is even more significant, with the normalized drain current decreasing by approximately four orders of magnitude. After 10 000 bending cycles with a 3 mm bending radius, the non-patterned TFTs stop exhibiting any on-current, which suggests that the devices have been physically damaged, and are not functional, which can be attributed to accumulated fatigue in the entire dielectric layer. However, in contrast to the non-patterned TFT, the patterned TFTs did not show any significant degradation even after 10 000 bending cycles, indicating that they are more robust and can maintain their electrical properties under repeated bending conditions. The results of the bending test clearly demonstrate the critical role of patterning in improving the mechanical reliability and durability of TFTs, particularly under repeated bending or flexing conditions, thereby highlighting the importance of patterning in TFTs. Organic semiconductors are renowned for

their flexibility but suffer from low mobility, low on/off ratios, and limitations arising from solution processing, such as large area uniformity, pin-hole, and voids. In contrast, inorganic semiconductors offer high mobility and on/off ratios but lack the flexibility required for future flexible applications (Table S2, Supporting Information).^[16,26,66–72] In this work, flexible TFT with high performance and excellent stability was achieved by combining inorganic semiconductors and organic gate dielectrics. Additionally, the stability of the flexible TFT could be further improved through a simple pattern process involving UV crosslinking of Parylene-OH.

A CMOS inverter is a fundamental logic circuit that serves as a building block for a wide range of applications. As basic elements of digital electronics, they play a crucial role in signal processing, logic operations, and the design of more complex circuits. CMOS inverters were fabricated on a glass substrate by combining an n-type IGZO with CL Parylene-OH and p-type tellurium (Te) with PEALD Al₂O₃; the schematic layout of the inverter is shown in Figure 5e. The electrical properties of Te TFT and their representative parameters are shown in Figure S17 and Table S1 (Supporting Information), respectively. The applied voltage (V_{DD}) was set from 2 to 10 V, while the input voltage (V_{in}) was set in the range of −10 to 10 V. Voltage transfer and gain curves of the proposed CMOS inverter with IGZO and Te are illustrated in Figure 5f,g, respectively. The output characteristics of the CMOS inverter were confirmed to be in full-swing mode with an inverter gain of 26.60 at a V_{DD} of 10 V. The CMOS inverter demonstrates the potential of realizing complex circuits for future electronics.

3. Conclusion

We reported the properties of Parylene-OH, including simple vacuum processability, high-k properties, and photoreactive nature. Parylene-OH exhibits a high dielectric constant of 6.05, which is twice that of the conventional Parylene family. Parylene-OH can be crosslinked by subjecting it to UV exposure, resulting in a higher dielectric constant of 7.53, without degradation of electrical properties, which is comparable to that of inorganic high-k dielectric Al₂O₃. Additionally, the crosslinking process enables the photopatterning of Parylene-OH, further enhancing its applicability in various electronic devices. CL Parylene-OH was employed in the fabrication of TFTs, flexible TFTs, and CMOS inverters, demonstrating its potential for use in electronic applications. With a unique combination of vacuum processability, robustness, high dielectric constant, photoreactive nature, and compatibility with flexible substrates, Parylene-OH can be considered a promising material for use in a wide range of applications, making it an attractive choice for future advancements in electronic technologies.

4. Experimental Section

Synthesis of 4-Hydroxy[2.2]Paracyclophane: The dimer used for synthesis was purchased from NURI TECH. Co. (Republic of Korea); [2.2]paracyclophane (≥99.0%). The materials utilized were as follows: Titanium(IV) chloride (ReagentPlus, 99.9%, Sigma Aldrich, USA), 1,1-dichlorodimethyl ether (97%, ACROS, USA), and hydrogen peroxide (35% in water, TCI, Japan) were used without any further processing. Sodium sulfate (98.5%),

dichloromethane (99.8%), methyl alcohol (99.8%), sulfuric acid (95.0%), n-hexane (99.5%), and ethyl acetate (99.5%) were purchased from SAMCHUN CHEMICALS (Republic of Korea). [2.2]Paracyclophane (3.00 g, 14.3 mmol) was dissolved in dichloromethane (200 mL) in a round bottom flask (RB) under nitrogen atmosphere. It was stirred for 1 h after titanium(IV) chloride (3.15 mL, 21.7 mmol) was added dropwise. 1, 1-Dichlorodimethyl ether (1.33 mL, 15 mmol) was added dropwise with methylene chloride and stirred for 1.5 h. Following quenching with water, the aqueous phase was extracted with dichloromethane, and the organic phase was dried over sodium sulfate. The crude product, 4-formyl[2.2]paracyclophane (3.04 g, 90%), was obtained as a colorless solid via rotary evaporation; ¹H NMR (CDCl₃, 600 MHz): δ 9.97 (1H, s), 7.04 (1H, d, J = 1.9 Hz), 6.75 (1H, dd, J = 7.7, 2.0 Hz), 6.62 (1H, d, J = 7.7 Hz), 6.59 (1H, dd, J = 7.7, 1.9 Hz), 6.52 (1H, dd, J = 7.8, 2.0 Hz), 6.45 (1H, dd, J = 7.9, 1.9 Hz), 6.40 (1H, dd, J = 7.9, 2.0 Hz), 4.13 (1H, ddd, J = 13.2, 10.2, 1.8 Hz), 3.29 (1H, ddd, J = 12.4, 10.2, 1.8 Hz), 3.25 – 3.18 (3H, m), 3.16 – 3.03 (4H, m), 2.98 (1H, ddd, J = 13.3, 10.4, 6.7 Hz); ¹³C NMR (CDCl₃, 151 MHz): δ 191.96, 143.25, 140.68, 139.52, 138.10, 136.61, 136.37, 136.14, 133.28, 132.94, 132.39, 132.18, 35.29, 35.17, 35.01, 33.64.

4-Formyl[2.2]paracyclophane (3.00 g, 12.7 mmol) was dissolved in dichloromethane (200 mL) and methanol (200 mL). Concentrated sulfuric acid (0.096 mL) and hydrogen peroxide (1.44 mL, 35% in water) were added and stirred at RT (25 °C) for 16 h. The solvent was removed using a rotary evaporator, and the residue was absorbed in dichloromethane (150 mL) and water (150 mL). The organic phase was dried over sodium sulfate and concentrated under reduced pressure. The crude product was purified via column chromatography (n-hexane and ethyl acetate). Finally, 4-hydroxy[2.2]paracyclophane was obtained as a yellowish solid (2.69 g, 95.17%); ¹H NMR (CDCl₃, 600 MHz): δ 7.03 (1H, dd, J = 7.8, 2.0 Hz), 6.58 (1H, dd, J = 7.8, 2.0 Hz), 6.47 (1H, dd, J = 7.9, 2.0 Hz), 6.45 – 6.39 (2H, m), 6.29 (1H, dd, J = 7.7, 1.7 Hz), 5.56 (1H, d, J = 1.7 Hz), 4.90 (1H, s, J = 513.0 Hz), 3.36 (1H, ddd, J = 13.7, 7.8, 4.4 Hz), 3.18 – 2.97 (6H, m), 2.93 (1H, ddd, J = 13.0, 10.1, 4.8 Hz), 2.74 – 2.65 (1H, m); ¹³C NMR (CDCl₃, 151 MHz) δ 153.66, 142.02, 139.64, 138.85, 135.47, 133.61, 132.78, 131.86, 127.96, 125.45, 125.04, 122.57, 35.32, 34.82, 33.84, 31.10.

Fabrication of Photopatterned Dielectric Layer: The CL Parylene-OH could be fabricated by (i) depositing the Parylene-OH via the CVD method and (ii) developing the dielectric layer via the photo-crosslinking process. (i) To fabricate the Parylene dielectric layer on the Al electrodes (S/D) and IGZO semiconductor, the Parylene thin film can be polymerized based on the Gorham method using custom-made Parylene CVD equipment (Teraleader, Republic of Korea). The Parylene-OH (250 mg) dimers sublimate to the vapor phase and were carried to the pyrolysis zone by inert argon gas, which ensures that they are radical-activated monomers. The temperature for dimers to sublimate was controlled depending on proximity to the pyrolysis zone, and the inner pressure was in the range of 0.10–0.15 Torr. Thereafter, monomers formed in this way moved onto the surface of the sample, which was placed on the rotating deposition holder in a chamber (80 °C). The deposition holder where the sample was placed was cooled to ≈5 °C. Once the CVD process was completed, the Parylene-OH could be deposited all over the device. (ii) Before irradiating with UV, the photomask was placed at the proper location. Thereafter, the Parylene-OH coating layer was irradiated with 254 nm wavelength for 10 min. The photomask was removed by rinsing it with toluene and ethanol for ≈5 s.

Material Characterization: The NMR and FTIR spectra were obtained using a 600 MHz FT-NMR (AVANCE III 600, Bruker), and Spectrum Two FTIR (Perkinelmer) for analyzing the synthesized dimer in the form of a KBr pellet, respectively. The custom-made CVD Polymerization equipment (ITS, Republic of Korea) was utilized to deposit the Parylene thin film. To confirm the chemical structure of Parylene thin film, DRIFT (Diffuse Reflection for Infrared Fourier Transform) spectroscopy was used and K-alpha+XPS (Thermo scientific) gave the clues about the difference between internal crosslinking and oxidation. For the characterization of crosslinked dimers, the TGA (N-1000, Sinco) was used to measure the chemical composition. The digital image showing the photopatterning process was captured by iPhone 11 pro (Apple). The OM image of the island and SEM tilted image letter-shaped CL Parylene-OH was obtained by OM (DM 2500, LEICA) and CLARA FE-SEM (TESCAN) respectively, indicating the high

pattern resolution and the boundaries of CL Parylene-OH. The sharpness of their boundaries and the surface roughness were characterized by AFM (NX7, XE-100, Park Systems). It was enough to understand that the quality of interface properties was great in TFTs architecture and MIM, so that any pin-hole, void, and mismatch was not observed by using FIB-SEM (Helios NanoLab, FEI) to show the cross-sectional image.

Fabrication Process for MIM, TFT Devices and Circuit: To fabricate IGZO with photopatternable Parylene-OH TFTs, glass was used as a substrate for both MIM and TFT, followed by ultrasonic cleaning with acetone and methanol for 10 min, respectively. For the MIM structure, 100-nm thick Al layers were deposited as the top and bottom electrodes via thermal evaporation. To fabricate IGZO TFTs, 30 nm thick a-IGZO active layers were deposited via radio frequency (RF) magnetron sputtering using a 3-inch IGZO target with an atomic composition of In:Ga:Zn = 1:1:1 at% (Toshiba, Japan) at room temperature on substrate. The working pressure was fixed at 3 mTorr and the Ar gas flow rate was 10 sccm. Thermal annealing was conducted at 300 °C for one hour in air ambient after depositing IGZO thin film. Subsequently, 100-nm thick Al layers were fabricated as source and drain electrodes using a thermal evaporation system. Post-deposition annealing was performed only after the deposition of the active layers. CL Parylene-OH was deposited as a gate insulator via CVD. Finally, 100 nm thick Al layers were thermally evaporated as the gate electrode. Except for the dielectric layers, all layers (active layer, source and drain electrodes, and gate electrode) were defined by a shadow mask. The patterning process for the dielectric layers was described above. The channel width and length of the IGZO TFTs were 800 and 200 μm, respectively. For the flexible TFTs, colorless polyimide (PI) was used as the substrate and 50 nm-thick Al₂O₃ was fabricated as the buffer layer via PEALD. The fabrication process for the IGZO TFTs containing the active material, gate dielectric (CL Parylene-OH), and source/drain/gate electrodes was the same as that for a rigid substrate. For CMOS circuits, IGZO TFTs were fabricated on a glass substrate, as described above. Once the IGZO TFTs were fabricated, Te was fabricated via sputtering, followed by annealing at 150 °C. Ni was deposited as the source/drain electrode for Te and connected to the NMOS and IGZO TFT via thermal evaporation. For Te, PEALD Al₂O₃ was deposited on top of Te as gate dielectric at 150 °C. Finally, the Al gate electrode was deposited and connected to the n-type TFT.

Density Functional Theory Calculation: All spin-polarized DFTs were performed using the VASP code.^[73,74] The exchange-correlation potential was estimated by the Perdew-Burke-Ernzerhof functional.^[74] The DFT-D3 van der Waals correction method with the Becke-Johnson damping model was consistently applied to all calculations to improve the reliability of the results.^[75] Valence electron wave functions were expanded on a plane-wave basis functions up to 400 eV cut-off kinetic energy.^[76] The convergence criteria for the electronic structure and atomic geometries were 10⁻⁸ eV and 0.05 eV·Å⁻¹, respectively. To improve the convergence of the states near the Fermi level, a Gaussian smearing function was used with a finite temperature window of 0.05 eV. The optimized single chain of Parylene-OH was stacked to construct a 3D Parylene-OH cell. The inter-chain distance was optimized. Two adjacent chains crosslinked with oxygen were pre-optimized and a 3D CL Parylene-OH cell was correspondingly constructed by stacking the optimized dual chains.

Density functional perturbation theory (DFPT) was employed to calculate static dielectric constant (ϵ_{static}).^[77-79] To estimate the ϵ_{static} of parylene, the following Equation 1 was used

$$\epsilon_{\text{static}} = \epsilon_0^{\alpha\beta}(\omega) = \epsilon_{\text{elec}}^{\alpha\beta}(\infty) + \epsilon_{\text{ion}}^{\alpha\beta}(\omega) \quad (1)$$

To calculate both components of the static dielectric constant, two independent calculations were performed to extract the electronic and ionic parts. The electronic part ($\epsilon_{\text{elec}}^{\alpha\beta}(\infty)$) was evaluated as a response to the external field perturbations, while the ionic part ($\epsilon_{\text{ion}}^{\alpha\beta}(\omega)$) was computed via the phonon frequencies at the Γ -point of the Brillouin zone. The electronic

contribution to the dielectric tensor $\epsilon_{\text{elec}}^{\alpha\beta}(\infty)$ determined by the following Equation 2 was obtained

$$\epsilon_{\text{elec}}^{\alpha\beta}(\infty) = 1 + 4\pi \frac{\partial P_{\alpha}}{\partial E_{\beta}} \quad (2)$$

where P_{α} is the component along the α direction of the induced polarization, ω is the angular frequency, and E_{β} represents the component along the β direction of the external field. The ionic part of the dielectric tensor was derived by following the Equation 3

$$\epsilon_{\text{ion}}^{\alpha\beta}(\omega) = \frac{4\pi}{\Omega} \sum_m \frac{S_m^{\alpha\beta}}{\omega_{m,q=0}^2 - \omega^2} \quad (3)$$

where Ω is the volume of the primitive cell, $S_m^{\alpha\beta}$ is the mode-dependent oscillator strength, and the m is phonon normal modes. The details of the method for extracting dielectric tensor are elsewhere.^[80,83]

The modern theory of polarization based on the Berry's phase approximation is applied to estimate the dipole moment. The total dipole moment is the sum of the dipole moments of the ionic and electronic dipoles. The ionic and the electronic dipole moment was estimated by the following Equations 4 and 5

$$D_{\text{ion}} = Z_{\text{val}} \cdot (r_{\text{atom}} - r_{\text{DIPOL}}) \quad (4)$$

$$D_{\text{electron}} = P_e \cdot V \quad (5)$$

where Z_{val} is the valence electron value denoting in the POTCAR of each atom, r_{atom} is the position of each atom, and r_{DIPOL} is the dipole center. P_e is the electronic part of polarization and V is the volume of the cell. The electronic contribution to polarization is expressed by

$$P_e = -\frac{f|e|}{\Omega} \sum_{n=1}^M \langle W_n | r | W_n \rangle \quad (6)$$

where W_n the Wannier function corresponds to the valence band n , and M is the occupied band. The equation is a general form of Berry's phase approximation.^[84]

Characterization of MIM, TFT Devices, and Circuit: All MIM, TFTs, and circuits were characterized at RT (≈ 25 °C) in the dark and ambient. Dielectric properties of MIM devices were measured using the Wayne Kerr 4100 LCR meter, while the electrical properties were measured using the Keithley 4200-SCS. The transfer curves and output curves of TFTs and transfer curves of CMOS circuits were measured using the Keithley 4200-SCS.

Supporting Information

Supporting Information is available from the Wiley Online Library or from the author.

Acknowledgements

This research was supported by the Commercialization Promotion Agency for R&D Outcomes (COMPA) funded by the Ministry of Science and ICT (MIST). (2022RMD-S03, development of parylene monomer with various functional groups for transistor and sensor applications) and also supported by the Basic Science Research Program through the National Research Foundation of Korea (NRF) funded by the Ministry of Education (Grant numbers: 2022R1A2C2008273, 2021R1A6A1A03043682, 2021M3F3A2A03017873, and RS-2023-00278208). This work was supported by the National Research Foundation of Korea (NRF) grant funded by the MIST (Grant numbers: RS-2022-00155706). This work was also supported by the Dongguk University Research Fund of 2023.

Conflict of Interest

The authors declare no conflict of interest.

Author Contributions

G.L. and S.C.J. contributed equally to this work. H.Y.K., H.-S.K., and K.J.L. supervised the project; G.L., S.C.J., J.-M.P., and B.N. explored theoretically the concepts and designed the experiments; G.L. and S.C.J. conducted all the experiments; G.L. performed the material characterization studies and S.C.J. did the electrical characterization studies; J.H.L. and H.C. gave the DFT calculation of the dielectric constant of Parylene materials; H.K. and D.H.K. analyzed mechanical properties of the parylene film; J.-M.P. and B.N. assisted with the experimental procedures; J.-M.P. and B.N. provided comments on the manuscript; G.L. and S.C.J. wrote the manuscript and revised the manuscript. All authors discussed the result and the manuscript.

Data Availability Statement

The data that support the findings of this study are available from the corresponding author upon reasonable request.

Keywords

flexible, oxide semiconductor, parylene, photopatternable, polymer dielectric

Received: March 31, 2024
Published online: April 22, 2024

- [1] K. Nomura, H. Ohta, A. Takagi, T. Kamiya, M. Hirano, H. Hosono, *Nature*. **2004**, 432, 488.
- [2] A. Liu, H. Zhu, S. Bai, Y. Reo, T. Zou, M.-G. Kim, Y.-Y. Noh, *Nat. Electron.* **2022**, 5, 78.
- [3] E. Guo, S. Xing, F. Dollinger, R. Hübner, S.-J. Wang, Z. Wu, K. Leo, H. Kleemann, *Nat. Electron.* **2021**, 4, 588.
- [4] J.-M. Park, H.-D. Kim, H. Joh, S. C. Jang, K. Park, Y. C. Park, H.-H. Nahm, Y.-H. Kim, S. Jeon, H.-S. Kim, *NPG Asia Mater.* **2020**, 12, 81.
- [5] J. Kim, S. C. Jang, K. Bae, J. Park, H. D. Kim, J. Lahann, H. S. Kim, K. J. Lee, *ACS Appl. Mater. Interfaces*. **2021**, 13, 43123.
- [6] B. Wang, W. Huang, L. Chi, M. Al-Hashimi, T. J. Marks, A. Facchetti, *Chem. Rev.* **2018**, 118, 5690.
- [7] T. E. Taourit, A. Meftah, N. Sengouga, M. Adaika, S. Chala, A. Meftah, *Nanoscale*. **2019**, 11, 23459.
- [8] Z. Lu, Y. Chen, W. Dang, L. Kong, Q. Tao, L. Ma, D. Lu, L. Liu, W. Li, Z. Li, *Nat. Commun.* **2023**, 14, 2340.
- [9] T. Li, T. Tu, Y. Sun, H. Fu, J. Yu, L. Xing, Z. Wang, H. Wang, R. Jia, J. Wu, *Nat. Electron.* **2020**, 3, 473.
- [10] J. O. Kim, J. S. Hur, D. Kim, B. Lee, J. M. Jung, H. A. Kim, U. J. Chung, S. H. Nam, Y. Hong, K. S. Park, *Adv. Funct. Mater.* **2020**, 30, 1906647.
- [11] J. Sheng, J. Park, D.-w. Choi, J. Lim, J.-S. Park, *ACS Appl. Mater. Interfaces*. **2016**, 8, 31136.
- [12] S. Hong, M. Mativenga, J. Jang, in 21st Int. Workshop Active-Matrix Flatpanel Displays Devices (AM-FPD), IEEE, Kyoto, Japan **2014**.
- [13] J. Wang, Q. Huang, Y. Gao, N. Shi, Q. Ge, H. Meng, M. Zhang, X. Wang, *Chem. Mater.* **2022**, 34, 9119.
- [14] P. Li, J. Yang, X. Ding, X. Li, J. Zhang, *IEEE J. Electron Devices Soc.* **2024**, 104, 063508.
- [15] K. Lu, J. Zhang, D. Guo, J. Xiang, Z. Lin, X. Zhang, T. Wang, H. Ning, R. Yao, J. Peng, *IEEE Electron Device Lett.* **2020**, 41, 417.
- [16] Z. Liang, W. Wu, X. Fu, H. Ning, W. Xu, X. Xiong, T. Qiu, C. Luo, R. Yao, J. Peng, *J. Phys. Chem.* **2023**, 14, 9245.
- [17] K.-W. Huang, T.-J. Chang, C.-Y. Wang, S.-H. Yi, C.-I. Wang, Y.-S. Jiang, Y.-T. Yin, H.-C. Lin, M.-J. Chen, *Mater. Sci. Semicond. Process.* **2020**, 109, 104933.
- [18] A. Rahmanudin, D. J. Tate, R. Marcial-Hernandez, N. Bull, S. K. Garlapati, A. Zamhuri, R. U. Khan, S. Faraji, S. R. Gollu, K. C. Persaud, *Adv. Electron. Mater.* **2020**, 6, 1901127.
- [19] T. Xu, Y. Liu, Y. Bu, S. Shu, S. Fan, M. Cao, T. Liu, J. Zou, J. Su, *Adv. Electron. Mater.* **2023**, 9, 2200984.
- [20] M. Seck, N. Mohammadian, A. K. Diallo, S. Faraji, M. Erouel, N. Bouguila, D. Ndiaye, K. Khirouni, L. A. Majewski, *Org. Electron.* **2020**, 83, 105735.
- [21] G. I. Kim, J. Jung, W. K. Min, M. S. Kim, S. Jung, D. H. Choi, J. Chung, H. J. Kim, *ACS Appl. Mater. Interfaces*. **2022**, 14, 28085.
- [22] Y. Gong, K. Zhao, L. Yan, W. Wei, C. Yang, H. Ning, S. Wu, J. Gao, G. Zhou, X. Lu, J. M. Liu, *IEEE Electron Device Lett.* **2018**, 39, 280.
- [23] L. Yan, W. He, X. Liang, C. Liu, X. Lu, C. Luo, A. Zhang, R. Tao, Z. Fan, M. Zeng, H. Ning, G. Zhou, X. Lu, J. M. Liu, *J. Mater. Chem. C*. **2020**, 8, 5163.
- [24] E. Carlos, J. Leppäniemi, A. Sneek, A. Alastalo, J. Deuermeier, R. Branquinho, R. Martins, E. Fortunato, *Adv. Electron. Mater.* **2020**, 6, 1901071.
- [25] R. N. Bukke, J. K. Saha, N. N. Mude, Y. Kim, S. Lee, J. Jang, *ACS Appl. Mater. Interfaces*. **2020**, 12, 35164.
- [26] N. Münzenrieder, L. Petti, C. Zysset, G. A. Salvatore, T. Kinkeldei, C. Perumal, C. Carta, F. Ellinger, G. Tröster, in 2012 International Electron Devices Meet, IEEE, San Francisco, CA, USA **2012**.
- [27] Y. Wang, X. Huang, T. Li, L. Li, X. Guo, P. Jiang, *Chem. Mater.* **2019**, 31, 2212.
- [28] Y. Yang, Y. Zhao, J. Liu, Z. Nie, J. Ma, M. Hua, Y. Zhang, X. Cai, X. He, *ACS Materials Lett.* **2020**, 2, 453.
- [29] J. H. Koo, J. Kang, S. Lee, J.-K. Song, J. Choi, J. Yoon, H. J. Park, S.-H. Sunwoo, D. C. Kim, W. Nam, *Nat. Electron.* **2023**, 6, 137.
- [30] J. Choi, C. Lee, C. Lee, H. Park, S. M. Lee, C.-H. Kim, H. Yoo, S. G. Im, *Nat. Commun.* **2022**, 13, 2305.
- [31] L. Krieg, F. Meierhofer, S. Gorny, S. Leis, D. Splith, Z. Zhang, H. von Wenckstern, M. Grundmann, X. Wang, J. Hartmann, *Nat. Commun.* **2020**, 11, 5092.
- [32] H.-Y. Chen, M. Hirtz, X. Deng, T. Laue, H. Fuchs, J. Lahann, *J. Am. Chem. Soc.* **2010**, 132, 18023.
- [33] Z. Hassan, D. Varadharajan, C. Zippel, S. Begum, J. Lahann, S. Bräse, *Adv. Mater.* **2022**, 34, 2201761.
- [34] Z.-Y. Guan, C.-Y. Wu, J.-T. Wu, C.-H. Tai, J. Yu, H.-Y. Chen, *ACS Appl. Mater. Interfaces*. **2016**, 8, 13812.
- [35] H.-Y. Chen, Y. Elkasabi, J. Lahann, *J. Am. Chem. Soc.* **2006**, 128, 374.
- [36] H. Park, J. Kwon, H. Ahn, S. Jung, *J. Mater. Chem. C*. **2019**, 7, 6251.
- [37] H. Ye, H.-j. Kwon, X. Tang, C. E. Park, T. K. An, S. H. Kim, *Org. Electron.* **2020**, 87, 105942.
- [38] E.-Y. Shin, E.-Y. Choi, Y.-Y. Noh, *Org. Electron.* **2017**, 46, 14.
- [39] J.-M. Park, H. Lee, G. Lee, S. C. Jang, Y. H. Chang, H. Hong, K.-B. Chung, K. J. Lee, D. H. Kim, H.-S. Kim, *ACS Appl. Mater. Interfaces*. **2023**, 15, 1525.
- [40] S. Pyo, H. Son, K.-Y. Choi, M. H. Yi, S. K. Hong, *Appl. Phys. Lett.* **2005**, 86, 133508.
- [41] J. S. Kwon, H. W. Park, D. H. Kim, Y.-J. Kwark, *ACS Appl. Mater. Interfaces*. **2017**, 9, 5366.
- [42] M. Vasilopoulou, A. M. Douvas, P. Argitis, *Mater. Chem. Phys.* **2012**, 135, 880.
- [43] Q. Shi, Y. Xie, S. Cai, W.-Y. Lee, Z. Bao, J. R. Matthews, K. L. Simonton, T. E. Myers, R. A. Bellman, M. He, *Org. Electron.* **2014**, 15, 991.
- [44] S. Wang, J. Xu, W. Wang, G.-J. N. Wang, R. Rastak, F. Molina-Lopez, J. W. Chung, S. Niu, V. R. Feig, J. Lopez, *Nature*. **2018**, 555, 83.

- [45] H. Park, S. Yoo, H. Ahn, J. Bang, Y. Jeong, M. Yi, J. C. Won, S. Jung, Y. H. Kim, *ACS Appl. Mater. Interfaces*. **2019**, 11, 45949.
- [46] W. F. Gorham, *J. Polym. Sci., Part A-1: Polym. Chem.* **1966**, 4, 3027.
- [47] C. J. Friedmann, S. Ay, S. Bräse, *J. Org. Chem.* **2010**, 75, 4612.
- [48] H. Yan, Z. Chen, Y. Zheng, C. Newman, J. R. Quinn, F. Dötz, M. Kastler, A. Facchetti, *Nature*. **2009**, 457, 679.
- [49] Y. Zhou, S.-T. Han, Z.-X. Xu, X.-B. Yang, H.-P. Ng, L.-B. Huang, V. Roy, *J. Mater. Chem.* **2012**, 22, 14246.
- [50] X. Yang, B. Geng, W. Peng, J. Li, J. Wei, K. Lan, X. Ren, G. Qin, *ACS Appl. Electron. Mater.* **2022**, 4, 2281.
- [51] H.-Y. Chen, J. Lahann, *Langmuir*. **2011**, 27, 34.
- [52] J. Lee, M. V. Maddipatla, A. Joy, B. D. Vogt, *Macromolecules*. **2014**, 47, 2891.
- [53] P. B. Jayatilaka, G. C. Pathiraja, A. Bandara, N. D. Subasinghe, N. Nanayakkara, *Can. J. Chem.* **2014**, 92, 809.
- [54] V. Santucci, F. Maury, F. Senocq, *Thin Solid Films*. **2010**, 518, 1675.
- [55] M. Gołda, M. Brzychczy-Włoch, M. Faryna, K. Engvall, A. Kotarba, *Mater. Sci. Eng. C*. **2013**, 33, 4221.
- [56] M. Golda-Cepa, K. Engvall, M. Hakkarainen, A. Kotarba, *Prog. Org. Coat.* **2020**, 140, 105493.
- [57] S. Kim, Y. Lee, M. Lee, S. An, S.-J. Cho, *Nanomaterials*. **2021**, 11, 1593.
- [58] H. Kweon, K.-Y. Choi, H. W. Park, R. Lee, U. Jeong, M. J. Kim, H. Hong, B. Ha, S. Lee, J.-Y. Kwon, *Nat. Commun.* **2022**, 13, 6775.
- [59] S. Diahm, M.-L. Locatelli, R. Khazaka, H. Hourdequin, R. Kumar, *IEEE Trans. Dielectr. Electr. Insul.* **2015**, 22, 2329.
- [60] A. Kachroudi, A. Kahouli, J. Legrand, F. Jomni, *J. Phys. Chem. A*. **2015**, 119, 6428.
- [61] M. Mokni, A. Kahouli, F. Jomni, J.-L. Garden, E. Andre, A. Sylvestre, *J. Phys. Chem. A*. **2015**, 119, 9210.
- [62] A. Kahouli, A. Sylvestre, F. Jomni, B. Yangui, J. Legrand, *J. Phys. Chem. A*. **2012**, 116, 1051.
- [63] K.-C. Ok, S.-H. K.o Park, C.-S. Hwang, H. Kim, H. S. Shin, J. Bae, J.-S. Park, *Appl. Phys.* **2014**, 36, 917.
- [64] K.-C. Ok, S. Oh, H.-J. Jeong, J. U. Bae, J.-S. Park, *IEEE Electron Device Lett.* **2015**, 36, 917.
- [65] H.-W. Jang, H.-R. Kim, J.-H. Yang, C.-W. Byun, S.-M. Yoon, in 2018 25th Int. Workshop Active-Matrix Flatpanel Displays Devices (AM-FPD), IEEE, Kyoto, Japan **2018**.
- [66] T. Q. Trung, N. T. Tien, Y. G. Seol, N.-E. Lee, *Org. Electron.* **2012**, 13, 533.
- [67] L. Han, K. Song, P. Mandlik, S. Wagner, *Appl. Phys. Lett.* **2010**, 96, 042111.
- [68] P.-Y. Liao, T.-C. Chang, W.-C. Su, Y.-J. Chen, B.-W. Chen, T.-Y. Hsieh, C.-Y. Yang, Y.-Y. Huang, H.-M. Chang, S.-C. Chiang, *Appl. Phys. Express*. **2016**, 9, 124101.
- [69] H.-H. Hsu, C.-Y. Chang, C.-H. Cheng, *IEEE Electron Device Lett.* **2013**, 34, 768.
- [70] K. Fukuda, Y. Takeda, M. Mizukami, D. Kumaki, S. Tokito, *Sci. Rep.* **2014**, 4, 3947.
- [71] X. Li, M. M. Billah, M. Mativenga, D. Geng, Y.-H. Kim, T.-W. Kim, Y.-G. Seol, J. Jang, *IEEE Electron Device Lett.* **2015**, 36, 811.
- [72] N. Munzenrieder, K. H. Cherenack, G. Troster, *IEEE Trans. Electron Devices*. **2011**, 58, 2041.
- [73] G. Kresse, J. Furthmüller, *Comput. Mater. Sci.* **1996**, 6, 15.
- [74] J. P. Perdew, K. Burke, M. Ernzerhof, *Phys. Rev.* **1996**, 77, 3865.
- [75] J. Klimeš, A. Michaelides, *J. Chem. Phys.* **2012**, 137, 120901.
- [76] G. Kresse, D. Joubert, *Phys. Rev. B*. **1999**, 59, 1758.
- [77] X. Gonze, C. Lee, *Phys. Rev. B*. **1997**, 55, 10355.
- [78] P. Giannozzi, S. De Gironcoli, P. Pavone, S. Baroni, *Phys. Rev. B*. **1991**, 43, 7231.
- [79] X. Wu, D. Vanderbilt, D. Hamann, *Phys. Rev. B*. **2005**, 72, 035105.
- [80] M. Gajdoš, K. Hummer, G. Kresse, J. Furthmüller, F. Bechstedt, *Phys. Rev. B*. **2006**, 73, 045112.
- [81] M. Bokdam, T. Sander, A. Stroppa, S. Picozzi, D. Sarma, C. Franchini, G. Kresse, *Sci. Rep.* **2016**, 6, 28618.
- [82] M. R. Osanloo, M. L. Van de Put, A. Saadat, W. G. Vandenberghe, *Nat. Commun.* **2021**, 12, 5051.
- [83] T. D. Huan, A. Mannodi-Kanakthodi, C. Kim, V. Sharma, G. Pilania, R. Ramprasad, *Sci. Data*. **2016**, 3, 160012.
- [84] R. King-Smith, D. Vanderbilt, *Phys. Rev. B*. **1993**, 47, 1651.